Journal of Computational Physics 235 (2013) 742–763

Contents lists available at SciVerse ScienceDirect

Journal of Computational Physics

journal homepage: www.elsevier.com/locate/jcp

A time and space correlated turbulence synthesis method for Large Eddy Simulations

Hugo G. Castro [a,*], Rodrigo R. Paz [b]

[a] Universidad Tecnológica Nacional (Facultad Regional Resistencia), Resistencia, Chaco, Argentina
[b] Consejo Nacional de Investigaciones Científicas y Técnicas (CONICET), Centro Internacional de Métodos Computacionales en Ingeniería (CIMEC), Instituto de Desarrollo Tecnológico para la Industria Química (INTEC), Universidad Nacional del Litoral (UNL), Santa Fe, Argentina

ARTICLE INFO

Article history:
Received 18 September 2011
Received in revised form 22 September 2012
Accepted 1 October 2012
Available online 17 November 2012

Keywords:
Turbulence synthesis
Inlet boundary conditions
Navier–Stokes equations
LES method

ABSTRACT

In the present work the problem of generating synthesized turbulence at inflow boundaries of the simulation domain is addressed in the context of the Large Eddy Simulation (LES) method. To represent adequately certain statistical properties of a turbulent process, we propose a synthesized turbulence methoz which is based on previous works (Huang et al., 2010; Smirnov et al., 2001) [15,28]. For this purpose, time and space correlations are introduced strictly in the mathematical formulation of the synthetic turbulence inflow data. It is demonstrated that the proposed approach inherits the properties of the methods on which it is based while presents some particular advantages as well.

The strategy of imposing conditions on the inlet velocity field through turbulence synthesis is implemented in the parallel multiphysics code called PETSc-FEM (http://www.cimec.org.ar/petscfem) primarily targeted to calculations throughout finite elements on general unstructured 2D and 3D grids. We present several numerical tests in order to validate and evaluate the method describing the dynamic phenomena that take place in "real-life" problems, such as a swirling turbulent flow inside a diffuser and the airflow around a vehicle model inside a wind tunnel at high Reynolds number.

1. Introduction

The generation of turbulent inflow boundary conditions for Large Eddy Simulations (LES) is a topic that has been widely studied owing to two main reasons. Firstly, LES has become an attractive approach due to the improvement of computational power. Secondly, a LES could demand a high execution time to obtain a fully developed turbulence if the inlet conditions are not properly prescribed, given that the flow behavior within the domain is strongly influenced by the inflow turbulence energy.

In view of these facts, several methods are available for the generation of inlet turbulence conditions and they follow different approaches that can be classified into two general methodologies [31]: precursor simulation methods and synthesis methods. Both approaches present advantages and drawbacks and can be implemented in many different ways.

Precursor simulation methods involve the generation of turbulence by running a precomputation of the simulated flow in order to generate a 'library' or database, before or in concurrency with LES. Then, the generated fluctuations are introduced at the inlet boundary of the computational domain. The relation precomputation/main-calculation can be linked in different ways. If the domain is quite large, the computational implementation through LES may become a difficult task, as it is in the case of a fully developed flow in a pipe. A possible solution is to reintroduce the flow out of a smaller domain into

* Corresponding author.
E-mail addresses: castrohgui@gmail.com (H.G. Castro), rodrigo.r.paz@gmail.com (R.R. Paz).

0021-9991/$ - see front matter © 2012 Elsevier Inc. All rights reserved.
http://dx.doi.org/10.1016/j.jcp.2012.10.035

the inlet by mapping the velocity components at the nodes. These *cyclic domains* methods allow to use a short section of the computational domain for the study of fully developed flows and have been used in the direct numerical simulation (DNS) of a turbulent channel flow [18] and in the LES of spatially developing boundary layers by modification of the Spalart method [24]. Another possibility is to generate a *preprepared library* by sampling the data at specific locations of an auxiliary domain (where turbulence precomputation takes place) and storing them for a later introduction into the LES domain as an inlet condition. In particular, Lund et al. [24] applied their modified Spalart method, in a *concurrent library generation* fashion, sampling the data as the simulation proceeds. An improvement of this methodology has been presented by Liu and Pletcher in [23].

All the precursor methodologies can be integrated into the main domain, sampling the turbulence in a downstream section and then mapping it back into the inlet [3]. Thus, the precursor simulation methods set the conditions for the LES implementation from a 'real' simulation of turbulence, hence, it is expected that the velocity fluctuation field could possess many of the required statistical characteristics, including energy spectrum, temporal and spatial correlation.

Another widely used methodology is the so called synthesized turbulence method. In this approach a pseudo-random coherent field of fluctuating velocities with spatial and time scales is superimposed on a predefined mean flow. The random perturbations can be generated in several different ways, such as the *Fourier techniques* (with its variants), the *digital filter based method* and the *proper orthogonal decomposition* (POD) analysis [31]. Fourier techniques are frequently implemented for the stochastic generation of turbulent velocities in a computationally efficient way in order to obtain time dependent turbulent fields satisfying statistical features. Basically, it consists of the generation of fluctuating time velocity series with random Fourier modes which are generally obtained by a Monte Carlo simulation with a specific target spectrum [20,22,21,28,15]. The digital filter method is a signal modeling through the use of linear non-recursive filters which is basically an implementation via digital filters of a Gaussian stochastic process (see [10,19]). Xie and Castro [38] proposed a modified form of this method, based on exponential (rather than Gaussian) velocity correlation functions for the simulation of street-scale flows. The third category is based on the use of POD to interpolate and extrapolate experimental data onto the domain inlet and to model the temporal and spatial characteristics of the flow [11]. This is probably the least expensive approach (computationally speaking) but with the requirement of a suitable experimental database from hot-wire, Laser Doppler Anemometry (LDA) or Particle Image Velocimetry (PIV) measurements [26].

A well known synthetic turbulence generator that employs Fourier techniques is the random flow generation (RFG) method proposed by Smirnov et al. [28]. Developed on the basis of the work of Kraichnan [21], this methodology involves scaling and orthogonal transformations where a transient flow field is generated in a three-dimensional domain as a superposition of harmonic functions with random coefficients. The method can generate an isotropic divergence-free fluctuating velocity field satisfying the Gaussian's spectral model as well as an inhomogeneous and anisotropic turbulence flow, provided that an anisotropic velocity correlation tensor is given. Smirnov et al. [28] used their approach to set inlet boundary conditions to LES methods in the simulation of turbulent fluctuations in a ship wake as well as initial boundary conditions in the simulation of turbulent flow around a ship-hull. Another application successfully tested by the authors was the particle dynamics modeling (see [29]). It must be noted that the RFG method has been included in the computational fluid dynamics (CFD) software FLUENT and was called *Spectral Synthesizer* [14].

The characteristics described above were taken into account in the method of Huang et al. [15], with the advantage that the spatially correlated turbulent flow field can satisfy any arbitrary model spectrum. This property is particularly useful in computational wind engineering applications where the von Kármán model is widely adopted as a target spectrum and the energy content of the inertial subrange cannot be discarded. Another remarkable feature of this method is its highly parallelizable algorithmic implementation since the generation of the fluctuating velocity series is independent for each node in the inlet plane of the computational domain; to the point that the procedure can be done in an embarrassingly parallel way. As this methodology implies discretizing and synthesizing procedures for the generation of the inlet turbulence the authors called this approach as *discretizing and synthesizing random flow generation* (DSRFG) method.

The results obtained by the application of the DSRFG method were compared with those of the RFG approach in the simulation of the atmospheric boundary layer flow over a prismatic building model [15]. The authors concluded that the DSRFG method proved to be able to enhance the accuracy of the turbulent flow simulation and wind-induced forces on the building since a more realistic vortices production in the inlet turbulence flow is performed. Nevertheless, only a few comments about the statistical characteristics of the synthesized turbulence were made while there was no discussion about time correlation.

The aim of the present study is to propose a synthesized turbulence methodology that is essentially a modification of the DSRFG method. We shall focus on the derivation of the mathematical equations used to generate fluctuating velocity series and the statistical implications of its parameters. In contrast to the DSRFG method, the proposed methodology makes possible to simulate velocity series with an energy content that matches the target values of the physical problem with a desired degree of accuracy. Furthermore, the inclusion of a time scale parameter in the formulation shows that a time scale range of variation can be obtained.

The organization of this paper is as follows. Section 2 is devoted to the description of the basic mathematical models used for the implementation of inlet turbulence flow conditions, such as spectra, spatial and temporal scales. A review of the DSRFG method is presented in Section 3. Then, a detailed derivation of the proposed modifications is performed introducing time and spatial correlations in the mathematical formulation of the velocity fluctuation series. The new approach is then validated in a test case representing an inhomogeneous anisotropic turbulent flow (Section 4). Finally, the simulation of a

turbulent flow over a simplified model vehicle in a wind tunnel is performed in Section 5 using the proposed method to generate the inlet boundary conditions. An extensive analysis and discussion of the obtained results is made.

2. Basic mathematical models describing inlet turbulence flow

2.1. Spectra

One of the characteristics of a turbulent flow is that the velocity field changes in a random fashion in the three space directions and time. The spatial two-point velocity correlation tensor R_{ij}, that is essential to any statistical representation of the turbulence behavior, is defined by

$$R_{ij}(\boldsymbol{r}) = \overline{u_i(\boldsymbol{x},t)u_j(\boldsymbol{x}+\boldsymbol{r},t)}, \tag{1}$$

where u_i is the i-th fluctuating velocity component and the over-bar indicates the expected value. The energy spectrum tensor Φ_{ij} of some velocity signal is defined as the Fourier transform of the autocorrelation function of that series [32],

$$\begin{aligned}\Phi_{ij}(\mathbf{k}) &= \frac{1}{(2\pi)^3}\iiint_{-\infty}^{+\infty}\exp(-i\mathbf{k}\cdot\boldsymbol{r})R_{ij}(\boldsymbol{r})\,d\boldsymbol{r},\\ R_{ij}(\boldsymbol{r}) &= \iiint_{-\infty}^{+\infty}\exp(i\mathbf{k}\cdot\boldsymbol{r})\Phi_{ij}(\mathbf{k})\,d\mathbf{k},\end{aligned} \tag{2}$$

where $\mathbf{k}$ is the wave vector. In particular, it can be seen that when $|\boldsymbol{r}| = 0$,

$$R_{ij}(0) = \overline{u_i(\boldsymbol{x},t)u_j(\boldsymbol{x},t)} = \iiint_{-\infty}^{+\infty}\Phi_{ij}(\mathbf{k})\,d\mathbf{k}, \tag{3}$$

showing that $\Phi_{ij}(\mathbf{k})$ represents a density function, in the wave-number space, of contributions to $\overline{u_i(\boldsymbol{x},t)u_j(\boldsymbol{x},t)} \equiv \overline{u_iu_j}$. In order to establish the amount of energy (per unit mass of the fluid) associated with any component of the fluctuating velocity it is necessary and sufficient to determine all components of the tensor $\overline{u_iu_j}$. Thus $\Phi_{ij}(\mathbf{k})$ describes a distribution of energy in $\mathbf{k}$-space [4] and the sum of the diagonal components of Φ_{ij} represents the kinetic energy at a given wave-number which is related to Eqs. (1) and (2) considering $\boldsymbol{r} = 0$ (Einstein summation convention is assumed),

$$R_{ii}(0) = \overline{u_iu_i} = \overline{u_1^2} + \overline{u_2^2} + \overline{u_3^2} = \iiint_{-\infty}^{+\infty}\Phi_{ii}(\mathbf{k})\,d\mathbf{k}. \tag{4}$$

Three-dimensional Fourier transforms are suitable for functions of vector arguments but, generally, measurements are made only with respect to one space coordinate. In such conditions a one-dimensional spectrum function $\Theta_{ij}(k_1)$ is obtained (i.e., a Fourier transform of the corresponding unidirectional velocity correlation function) which can be derived by integrating the spectrum tensor Φ_{ij} over the lateral wave vector components. This spectrum function is generally called "longitudinal" spectrum if the direction coincides with x_1 coordinate direction or "lateral" spectrum if it corresponds to the x_2 or x_3 coordinate direction. As an example, the equation for a one-dimensional longitudinal spectrum is

$$\begin{aligned}\Theta_{11}(k_1) &= \frac{1}{2\pi}\int_{-\infty}^{+\infty}R_{11}(r_1,0,0)\exp(-ik_1r_1)\,dr_1,\\ &= \iint_{-\infty}^{+\infty}\Phi_{11}(k_1,k_2,k_3)\,dk_2\,dk_3.\end{aligned} \tag{5}$$

If we integrate $R_{ij}(\boldsymbol{r})$ and $\Phi_{ij}(\mathbf{k})$ over spherical shells of radius $r = |\boldsymbol{r}|$ and $k = |\mathbf{k}|$, respectively,

$$\begin{aligned}S_{ij}(r) &= \frac{1}{4\pi r^2}\oiint R_{ij}(\boldsymbol{r})\,d\boldsymbol{\sigma}(r),\\ \Psi_{ij}(k) &= \oiint\Phi_{ij}(\mathbf{k})\,d\boldsymbol{\sigma}(k),\end{aligned} \tag{6}$$

where $d\boldsymbol{\sigma}$ is the surface element of the shell, we obtain functions of the position vector magnitude r and the wave vector magnitude k (i.e., the wave number). $S_{ij}(r)$ represents an average correlation tensor and $\Psi_{ij}(k)$ the energy contribution from wave numbers between k and $k+dk$ to the energy tensor $\overline{u_iu_j}$. Particularly, integrating $\Phi_{ii}(\mathbf{k})$ over a spherical shell, i.e.,

$$E(k) = \frac{1}{2}\Psi_{ii}(k) = \frac{1}{2}\oiint\Phi_{ii}(\mathbf{k})\,d\boldsymbol{\sigma}, \tag{7}$$

the total energy at a wave number k is obtained. That is, the integral of the *energy spectrum function* $E(k)$ is equal to the kinetic energy per unit mass of fluid:

$$\int_0^\infty E(k)dk = \frac{1}{2}\int_0^\infty\left[\oiint\Phi_{ii}(\mathbf{k})\,d\boldsymbol{\sigma}\right] = \frac{1}{2}\iiint_{-\infty}^{\infty}\Phi_{ii}(\mathbf{k})\,d\mathbf{k} = \frac{1}{2}\overline{u_iu_i}. \tag{8}$$

In isotropic turbulence the energy spectrum function $E(k)$ is somewhat different to the one-dimensional spectrum $\Theta_{11}(k_1)$, which has its maximum value at $k_1 = 0$, while the spherically averaged spectrum approaches to zero as $k \to 0$ [13], see Fig. 1.

The importance of defining a one-dimensional spectrum lies in its application to the experimental field since it can be measured as a frequency spectrum at a fixed point and then transformed to a spatial spectrum according to Taylor's hypothesis (frozen turbulence approximation).

2.2. Integral length scale

Integral scales of turbulence can be considered as measures of the average size of the eddies present in the turbulent flow. For an isotropic and homogeneous turbulent velocity field the integral length scales based on the two point correlations along the direction j are defined as

$$L_{ik,j}(\boldsymbol{x}) = \int_0^\infty \frac{\overline{u_i(\boldsymbol{x})u_k(\boldsymbol{x}+r\mathbf{e}_j)}}{\overline{u_i(\boldsymbol{x})u_k(\boldsymbol{x})}}\,dr, \tag{9}$$

where $\mathbf{e}_j$ is the unit vector in the j-direction. When the correlation and velocity directions are aligned, e.g. for $L_{11,1}$, a longitudinal integral scale is obtained:

$$L_{11,1} = \int_0^\infty \frac{\overline{u_1 u_1(r_1)}}{\overline{u_1^2}}\,dr_1 = \frac{1}{\overline{u_1^2}}\int_0^\infty R_{11}(r_1,0,0)\,dr_1, \tag{10}$$

where independence of the position $\boldsymbol{x}$ has been introduced. Interestingly, the values of the one-dimensional spectra at zero wave number determine the integral scales of the turbulence field, i.e., if in Eq. (5) $k_1 = 0$ then,

$$\Theta_{11}(0) = \frac{1}{2\pi}\int_{-\infty}^{+\infty} R_{11}(r_1,0,0)\,dr_1 = \frac{\overline{u_1^2}}{\pi}L_{11,1}, \tag{11}$$

having used Eq. (10) and given that R_{11} is an even function.

2.3. Time scale

The spectra defined in Section 2.1 are related to velocity correlations taken from two different points in space at the same time. If a fixed point in space is considered, a Fourier transform of the correlation function of a varying time delay defines the time spectra $\psi_{ij}(\omega)$ [32]:

$$R_{ij} = \overline{u_i(\boldsymbol{x},t)u_j(\boldsymbol{x},t+\tau)} = \int_{-\infty}^{\infty} \exp(i\omega\tau)\psi_{ij}(\omega)\,d\omega,$$

where

$$\psi_{ij}(\omega) = \frac{1}{2\pi}\int_{-\infty}^{\infty} \exp(-i\omega\tau)R_{ij}(\tau)\,d\tau.$$

In homogeneous turbulence, the value of $\mathrm{tr}(\psi_{ij}(\omega))$ at $\omega = 0$ defines the integral time scale:

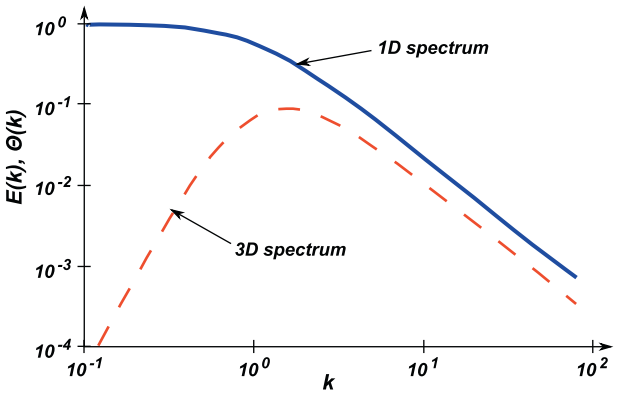

Fig. 1. Comparison between one-dimensional and three-dimensional von Kármán spectra [13].

$$\psi_{ii}(0) = \frac{1}{2\pi}\int_{-\infty}^{\infty} R_{ii}(\tau)\,d\tau = \frac{T}{\pi}\overline{u_i u_i}, \tag{12}$$

where T is the Eulerian integral time scale.

3. A modified method to synthesize inlet turbulence

Huang et al. [15] proposed a turbulence synthesis method called discretizing and synthesizing random flow generation (DSRFG) for the implementation of inlet turbulence conditions to perform LES. This method proved to have several advantages with respect to its predecessor, the random flow generation (RFG) by Smirnov et al. [28]. Nevertheless, some re-analysis of the DSRFG equations performed by the authors of this work demonstrates that some improvements can be made. According to this, a brief description of the DSRFG method is performed in this section along with the introduction of the proposed modifications. For a more detailed discussion about the RFG and DSRFG methods, the reader is encouraged to refer to the original articles [28,15].

Following the DSRFG method, a homogeneous and isotropic turbulent flow field $\boldsymbol{u}(\boldsymbol{x},t)$ can be synthesized as follows:

$$u_i(\boldsymbol{x},t) = \sum_{m=1}^{M}\sum_{n=1}^{N}[p_i^{m,n}\cos(\tilde{k}_j^{m,n}\tilde{x}_j + \omega_{m,n}t) + q_i^{m,n}\sin(\tilde{k}_j^{m,n}\tilde{x}_j + \omega_{m,n}t)], \tag{13}$$

where

$$\mathbf{p}^{m,n} = \frac{\zeta\times\mathbf{k}^{m,n}}{|\zeta\times\mathbf{k}^{m,n}|}\sqrt{a\frac{4E(k_m)}{N}}, \tag{14}$$

$$\mathbf{q}^{m,n} = \frac{\xi\times\mathbf{k}^{m,n}}{|\xi\times\mathbf{k}^{m,n}|}\sqrt{(1-a)\frac{4E(k_m)}{N}}, \tag{15}$$

$$\tilde{\mathbf{x}} = \frac{\mathbf{x}}{L_s}, \tag{16}$$

$$\tilde{\mathbf{k}}^{m,n} = \frac{\mathbf{k}^{m,n}}{k_0}, \tag{17}$$

with $\omega_{m,n}\in N(0,2\pi f_m)$, $f_m = k_m U_{\text{avg}}$, a is a random number uniformly distributed between 0 and 1, ζ and ξ are the vector form of ζ_i^n and ξ_i^n, which are random numbers selected independently from $N(0,1)$. In Eqs. (16) and (17) L_s is a scale factor related to the length scale of turbulence and k_0 is the lowest wavenumber of the discrete spectrum.

The factors $p_i^{m,n}$ and $q_i^{m,n}$ define the distribution of the three dimensional energy spectrum $E(k_m)$ in each of the spatial coordinate axes which in turn are functions of the space wave number $\mathbf{k}^{m,n}$ ($|\mathbf{k}^{m,n}| = k_m$) and normal random vectors ζ and ξ. When dealing with homogeneous and isotropic turbulence, the distribution of $\mathbf{k}^{m,n}$ is isotropic on the surface of a sphere and consequently the energy is uniformly distributed in space. In such conditions it is evident that the same spectrum will be obtained in the three principal directions but in the case of inhomogeneous and anisotropic turbulence the distribution of $\mathbf{k}^{m,n}$ must change according to the conditions of inhomogeneity and anisotropy. To achieve this behavior, $p_i^{m,n}$ and $q_i^{m,n}$ must be *aligned* with the energy spectrum along a principal direction and then the distribution of $\mathbf{k}^{m,n}$ can be *remapped* on the surface of the sphere. To summarize, the method is implemented using Eq. (13) and

$$p_i^{m,n} = \text{sign}(r_i^{m,n})\sqrt{\frac{4}{N}E_i(k_m)\frac{(r_i^{m,n})^2}{1+(r_i^{m,n})^2}}, \tag{18}$$

$$q_i^{m,n} = \text{sign}(r_i^{m,n})\sqrt{\frac{4}{N}E_i(k_m)\frac{1}{1+(r_i^{m,n})^2}}, \tag{19}$$

$$\mathbf{k}^{m,n}\cdot\mathbf{p}^{m,n} = 0, \tag{20}$$

$$\mathbf{k}^{m,n}\cdot\mathbf{q}^{m,n} = 0, \tag{21}$$

$$|\mathbf{k}^{m,n}| = k_m, \tag{22}$$

where $r_i^{m,n}$ is a random number, independently selected from a three dimensional Normal distribution with $\mu_r = 0$ and $\sigma_r = 1$.

In the following, we made some considerations about the statistical implications of the DSRFG method with the aim to expose the concepts behind the modifications that are to be introduced later. The mean square value of a random function $f(t)$ is defined as [6]:

$$f^2_{\mathrm{rms}}(t) = \lim_{T\to\infty}\frac{1}{T}\int_0^T f^2(t)\,dt \tag{23}$$

and regarding Eq. (13), we have in each direction $i = 1,2,3$:

$$u^2_{\mathrm{rms},i}(\boldsymbol{x},t) = \lim_{T\to\infty}\frac{1}{T}\int_0^T \left\{\sum_{m=1}^{M}\sum_{n=1}^{N}[p_i^{m,n}\cos(\tilde{k}_j^{m,n}\tilde{x}_j + \omega_{m,n}t) + q_i^{m,n}\sin(\tilde{k}_j^{m,n}\tilde{x}_j + \omega_{m,n}t)]\right\}^2 dt. \tag{24}$$

Defining,

$$\begin{aligned}\alpha_{m,n} &= p_i^{m,n}\cos(\tilde{k}_j^{m,n}\tilde{x}_j + \omega_{m,n}t),\\ \varphi_{m,n} &= q_i^{m,n}\sin(\tilde{k}_j^{m,n}\tilde{x}_j + \omega_{m,n}t),\end{aligned} \tag{25}$$

and noting that

$$\begin{aligned}\left[\sum_{m=1}^{M}\sum_{n=1}^{N}(\alpha_{m,n}+\varphi_{m,n})\right]^2 &= \left(\sum_{m=1}^{M}\sum_{n=1}^{N}\alpha_{m,n} + \sum_{m=1}^{M}\sum_{n=1}^{N}\varphi_{m,n}\right)^2\\ &= \left(\sum_{m=1}^{M}\sum_{n=1}^{N}\alpha_{m,n}\right)^2 + 2\sum_{m=1}^{M}\sum_{n=1}^{N}\sum_{r=1}^{M}\sum_{s=1}^{N}\alpha_{m,n}\varphi_{r,s} + \left(\sum_{m=1}^{M}\sum_{n=1}^{N}\varphi_{m,n}\right)^2,\end{aligned} \tag{26}$$

Eq. (24) can be written as

$$\lim_{T\to\infty}\frac{1}{T}\int_0^T\left[\sum_{m=1}^{M}\sum_{n=1}^{N}(\alpha_{m,n}+\varphi_{m,n})\right]^2 dt = \lim_{T\to\infty}\frac{1}{T}\int_0^T\left(\sum_{m=1}^{M}\sum_{n=1}^{N}\alpha_{m,n}\right)^2 dt + \lim_{T\to\infty}\frac{1}{T}\int_0^T\left(\sum_{m=1}^{M}\sum_{n=1}^{N}\varphi_{m,n}\right)^2 dt, \tag{27}$$

where the following integration result was used:

$$\begin{aligned}\lim_{T\to\infty}\frac{1}{T}\int_0^T \alpha_{m,n}\varphi_{r,s}\,dt &= p_i^{m,n}q_i^{r,s}\lim_{T\to\infty}\frac{1}{T}\int_0^T \cos(\tilde{k}_j^{m,n}\tilde{x}_j + \omega_{m,n}t)\sin(\tilde{k}_j^{r,s}\tilde{x}_j + \omega_{r,s}t)\,dt\\ &= p_i^{m,n}q_i^{r,s}\lim_{T\to\infty}\frac{1}{2T(\omega_{r,s}+\omega_{m,n})}\{-\cos[(\tilde{k}_j^{r,s}+\tilde{k}_j^{m,n})\tilde{x}_j + (\omega_{r,s}+\omega_{m,n})t] - \cos[(\tilde{k}_j^{r,s}-\tilde{k}_j^{m,n})\tilde{x}_j\\ &\quad + (\omega_{r,s}-\omega_{m,n})t]\}_0^T = 0.\end{aligned} \tag{28}$$

Furthermore, Eq. (27) can be rewritten as

$$\begin{aligned}\lim_{T\to\infty}\frac{1}{T}\int_0^T\left[\sum_{m=1}^{M}\sum_{n=1}^{N}(\alpha_{m,n}+\varphi_{m,n})\right]^2 dt &= \lim_{T\to\infty}\frac{1}{T}\int_0^T\left(\sum_{m=1}^{M}\sum_{n=1}^{N}\alpha_{m,n}^2 + \sum_{m=1}^{M}\sum_{\substack{n=1\\ m\neq r,n\neq s}}^{N}\sum_{r=1}^{M}\sum_{s=1}^{N}\alpha_{m,n}\alpha_{r,s}\right)dt\\ &\quad + \lim_{T\to\infty}\frac{1}{T}\int_0^T\left(\sum_{m=1}^{M}\sum_{n=1}^{N}\varphi_{m,n}^2 + \sum_{m=1}^{M}\sum_{\substack{n=1\\ m\neq r,n\neq s}}^{N}\sum_{r=1}^{M}\sum_{s=1}^{N}\varphi_{m,n}\varphi_{r,s}\right)dt\\ &= \lim_{T\to\infty}\frac{1}{T}\sum_{m=1}^{M}\sum_{n=1}^{N}\int_0^T\alpha_{m,n}^2 dt + \lim_{T\to\infty}\frac{1}{T}\sum_{m=1}^{M}\sum_{n=1}^{N}\int_0^T\varphi_{m,n}^2 dt,\end{aligned} \tag{29}$$

where the terms

$$\begin{aligned}&\lim_{T\to\infty}\frac{1}{T}\int_0^T\sum_{m=1}^{M}\sum_{\substack{n=1\\ m\neq r,n\neq s}}^{N}\sum_{r=1}^{M}\sum_{s=1}^{N}\alpha_{m,n}\alpha_{r,s}\,dt,\\ &\lim_{T\to\infty}\frac{1}{T}\int_0^T\sum_{m=1}^{M}\sum_{\substack{n=1\\ m\neq r,n\neq s}}^{N}\sum_{r=1}^{M}\sum_{s=1}^{N}\varphi_{m,n}\varphi_{r,s}\,dt,\end{aligned} \tag{30}$$

vanish as $T\to\infty$. Then, using the result of Eq. (29) and by virtue of Eqs. (24) and (25):

$$\begin{aligned}u^2_{\mathrm{rms},i}(\boldsymbol{x},t) &= \lim_{T\to\infty}\frac{1}{T}\int_0^T\left[\sum_{m=1}^{M}\sum_{n=1}^{N}(\alpha_{m,n}+\varphi_{m,n})\right]^2 dt\\ &= \lim_{T\to\infty}\frac{1}{T}\sum_{m=1}^{M}\sum_{n=1}^{N}[p_i^{m,n}]^2\int_0^T[\cos(\tilde{k}_j^{m,n}\tilde{x}_j+\omega_{m,n}t)]^2dt + \lim_{T\to\infty}\frac{1}{T}\sum_{m=1}^{M}\sum_{n=1}^{N}[q_i^{m,n}]^2\int_0^T[\sin(\tilde{k}_j^{m,n}\tilde{x}_j+\omega_{m,n}t)]^2dt\\ &= \frac{1}{2}\sum_{m=1}^{M}\sum_{n=1}^{N}[p_i^{m,n}]^2 + \frac{1}{2}\sum_{m=1}^{M}\sum_{n=1}^{N}[q_i^{m,n}]^2.\end{aligned} \tag{31}$$

Now, summing the left and right hands for $i = 1,2,3$,

$$\sum_{i=1}^{3} u_{\mathrm{rms},i}^2(\boldsymbol{x},t) = \frac{1}{2}\sum_{m=1}^{M}\sum_{n=1}^{N}\sum_{i=1}^{3}[p_i^{m,n}]^2 + \frac{1}{2}\sum_{m=1}^{M}\sum_{n=1}^{N}\sum_{i=1}^{3}[q_i^{m,n}]^2, \tag{32}$$

or in a more compact form (using Einstein summation convention):

$$\overline{u_i u_i} = \frac{1}{2}\sum_{m=1}^{M}\sum_{n=1}^{N} p_i^{m,n} p_i^{m,n} + \frac{1}{2}\sum_{m=1}^{M}\sum_{n=1}^{N} q_i^{m,n} q_i^{m,n} = 2\int_0^\infty E(k)\,dk \approx 2\sum_{m=1}^{M} E(k_m)\Delta k_m, \tag{33}$$

where the result of Eq. (8) was used. According to the definition of $p_i^{m,n}$ and $q_i^{m,n}$, Eqs. (18) and (19), it can be seen that

$$\overline{u_i u_i} = \frac{1}{2}\sum_{m=1}^{M}\sum_{n=1}^{N}\sum_{i=1}^{3}\left[\frac{4}{N}E_i(k_m)\frac{(r_i^{m,n})^2}{1+(r_i^{m,n})^2} + \frac{4}{N}E_i(k_m)\frac{1}{1+(r_i^{m,n})^2}\right] = \frac{2}{N}\sum_{m=1}^{M}\sum_{n=1}^{N} E(k_m) = 2\sum_{m=1}^{M} E(k_m), \tag{34}$$

thus, as $E(k_m)$ is a positive quantity for any k, the kinetic energy is represented by a divergent series. This causes a strong dependence of the rms values of the generated fluctuating velocities on the number of points M considered to discretize the model spectrum.

3.1. Time and spatial correlation

The time autocorrelation function gives information about how correlated is the signal at two different times and its connection to the time spectra was pointed out in Section 2.3. Following Eqs. (13) and (23) the autocorrelation function can be computed as

$$\begin{aligned}\overline{u_i(\boldsymbol{x},t)u_i(\boldsymbol{x},t+\tau)} = \lim_{T\to\infty}\frac{1}{T}\int_0^T u_i(\boldsymbol{x},t)u_i(\boldsymbol{x},t+\tau)\,dt = \lim_{T\to\infty}\frac{1}{T}\int_0^T \sum_{m=1}^{M}\sum_{n=1}^{N}\Big[p_i^{m,n}\cos(\tilde{k}_j^{m,n}\tilde{x}_j+\omega_{m,n}t)+\\ +q_i^{m,n}\sin(\tilde{k}_j^{m,n}\tilde{x}_j+\omega_{m,n}t)\Big]\sum_{m=1}^{M}\sum_{n=1}^{N}\Big[p_i^{m,n}\cos(\tilde{k}_j^{m,n}\tilde{x}_j++\omega_{m,n}(t+\tau))+q_i^{m,n}\sin(\tilde{k}_j^{m,n}\tilde{x}_j+\omega_{m,n}(t+\tau))\Big]dt,\end{aligned} \tag{35}$$

then, after some mathematical manipulation using Eqs. (18) and (19),

$$\begin{aligned}\overline{u_i(\boldsymbol{x},t)u_i(\boldsymbol{x},t+\tau)} &= \sum_{m=1}^{M}\sum_{n=1}^{N}\left[(p_i^{m,n})^2\frac{\cos(\tau\omega_{m,n})}{2} + p_i^{m,n}q_i^{m,n}\frac{\sin(\tau\omega_{m,n})}{2} - p_i^{m,n}q_i^{m,n}\frac{\sin(\tau\omega_{m,n})}{2} + (q_i^{m,n})^2\frac{\cos(\tau\omega_{m,n})}{2}\right]\\ &= \sum_{m=1}^{M}\sum_{n=1}^{N}\frac{2}{N}E_i(k_m)\cos(\tau\omega_{m,n}).\end{aligned} \tag{36}$$

Note that, if $\tau = 0$ then Eq. (36) gives back Eq. (31).

Likewise, an expression for the spatial correlation can be obtained in an analogous way:

$$\overline{u_i(\boldsymbol{x},t)u_i(\boldsymbol{x}',t)} = \sum_{m=1}^{M}\sum_{n=1}^{N}(p_i^{m,n})^2\frac{\cos[\tilde{k}_j^{m,n}(\tilde{x}'_j-\tilde{x}_j)]}{2} + (q_i^{m,n})^2\frac{\cos[\tilde{k}_j^{m,n}(\tilde{x}'_j-\tilde{x}_j)]}{2} = \sum_{m=1}^{M}\sum_{n=1}^{N}\frac{2}{N}E_i(k_m)\cos\left[\tilde{k}_j^{m,n}\frac{(x'_j-x_j)}{L_s}\right] \tag{37}$$

Comparing Eqs. (36) and (37), it can be seen that while in Eq. (37) a *scaling parameter* L_s (that provides a way to obtain the required spatial correlation in the generated flow field) exists, there is not an analogous parameter in Eq. (36).

3.2. Proposed methodology

In the light of the analysis above, we propose some modifications to the equations of the DSRFG method. Firstly, the Fourier series in Eq. (13) will be written as:

$$u_i(\boldsymbol{x},t) = \sum_{m=1}^{M}\sum_{n=1}^{N}\left[p_i^{m,n}\cos\left(\tilde{k}_j^{m,n}\tilde{x}_j + \omega_{m,n}\frac{t}{\tau_0}\right) + q_i^{m,n}\sin\left(\tilde{k}_j^{m,n}\tilde{x}_j + \omega_{m,n}\frac{t}{\tau_0}\right)\right]. \tag{38}$$

The inclusion of a parameter that modifies the time t is based on the work of Smirnov et al. [28] and Batten et al. [5] but with a different physical meaning: here, τ_0 is not the turbulence time scale but a dimensionless parameter introduced in Eq. (38) to allow some "control" over the time correlation of the generated velocity series.

As it was previously shown by Eq. (33), the turbulent flow energy is related to the three dimensional energy spectrum $E(k_m)$ and the factors $p_i^{m,n}$ and $q_i^{m,n}$. As stated in [15], these factors align the energy spectrum according to the anisotropy conditions of the turbulence, providing a synthesized velocity series that must satisfy the mean square values on each spatial direction. Starting from these considerations and noticing that from Eq. (34) the kinetic energy is not approximated by a convergent series, it is required an alternative analysis to ensure that the synthetic turbulence intensity can represents adequately the flow to be simulated. In this work we perform a simple "decoupling" over Eq. (33), using the following relationship:

$$\sum_{i=1}^{3} u_{\mathrm{rms},i}^2 = 2\sum_{m=1}^{M} E(k_m)\Delta k_m = 2\sum_{m=1}^{M}\sum_{i=1}^{3} c_i E_i(k_m)\Delta k_m. \tag{39}$$

This equation implies that the three-dimensional energy spectrum $E(k)$ is a weighted sum of modified one-dimensional energy spectra aligned with the three principal directions. Some discussion about the consequences of this representation will be given in Section 4.

In Eq. (39) c_i is a function value that depends on the form of the spectrum in order to satisfy the condition

$$u_{\mathrm{rms},i}^2 = 2c_i \int_0^{\infty} E_i(k)\, dk, \tag{40}$$

i.e., in each direction the variance of the simulated velocity series must satisfy Eq. (40). Then,

$$\sum_{i=1}^{3} u_{\mathrm{rms},i}^2 = 2\sum_{i=1}^{3} \int_0^{\infty} c_i E_i(k)\Delta k = 2\int_0^{\infty} E(k)\Delta k. \tag{41}$$

Thereby, for each direction i we obtain the modified version of Eqs. (18) and (19):

$$p_i^{m,n} = \mathrm{sign}(r_i^{m,n})\sqrt{\frac{4c_i}{N} E_i(k_m)\Delta k_m \frac{(r_i^{m,n})^2}{1+(r_i^{m,n})^2}}, \tag{42}$$

$$q_i^{m,n} = \mathrm{sign}(r_i^{m,n})\sqrt{\frac{4c_i}{N} E_i(k_m)\Delta k_m \frac{1}{1+(r_i^{m,n})^2}}. \tag{43}$$

Now Eq. (36) can be written as

$$\overline{u_i(\boldsymbol{x},t)u_i(\boldsymbol{x},t+\tau)} = \frac{2c_i}{N}\sum_{m=1}^{M}\sum_{n=1}^{N} E_i(k_m)\Delta k_m \cos\left(\frac{\tau}{\tau_0}\omega_{m,n}\right), \tag{44}$$

while Eq. (37) changes to

$$\overline{u_i(\boldsymbol{x},t)u_i(\boldsymbol{x}',t)} = \frac{2c_i}{N}\sum_{m=1}^{M}\sum_{n=1}^{N} E_i(k_m)\Delta k_m \cos\left[\tilde{k}_j^{m,n}\frac{(x_j'-x_j)}{L_s}\right]. \tag{45}$$

As in the DSRFG method, the spatial scaling parameter L_s is computed as

$$L_s = \theta_1\sqrt{L_u^2+L_v^2+L_w^2}, \tag{46}$$

while the dimensionless time-correlation parameter τ_0 is a scalar quantity. Since this new methodology is based on the DSRFG approach, we called it as *modified discretizing and synthesizing random flow generation* (MDSRFG).

4. Validation of the procedure

The first test performed is the simulation of an inhomogeneous anisotropic turbulent flow field. This example was proposed by Huang et al. in [15]. The spectra of the three principal velocity components are described by the von Kármán models:

$$S_u(f) = \frac{4(I_u U_{\mathrm{avg}})^2 (L_u/U_{\mathrm{avg}})}{[1+70.8(fL_u/U_{\mathrm{avg}})^2]^{5/6}}, \tag{47}$$

$$S_v(f) = \frac{4(I_v U_{\mathrm{avg}})^2 (L_v/U_{\mathrm{avg}})[1+188.4(2fL_v/U_{\mathrm{avg}})^2]}{[1+70.8(2fL_v/U_{\mathrm{avg}})^2]^{11/6}}, \tag{48}$$

$$S_w(f) = \frac{4(I_w U_{\mathrm{avg}})^2 (L_w/U_{\mathrm{avg}})[1+188.4(2fL_w/U_{\mathrm{avg}})^2]}{[1+70.8(2fL_w/U_{\mathrm{avg}})^2]^{11/6}}. \tag{49}$$

The turbulence intensity values are $I_u = 8\%$, $I_v = 16\%$ and $I_w = 24\%$, while the turbulence integral length scales are $L_u = 0.6$ m, $L_v = 0.3$ m and $L_w = 0.1$ m. To apply the procedure we must first obtain the c_i values in Eqs. (42) and (43) using the relationship (40), that is

$$u_{\mathrm{rms},1}^2 = (I_u U_{\mathrm{avg}})^2 = 2c_1 \int_0^{\infty} S_u(k)\, dk \approx 2c_1\, 0.2377\, \beta\left(\frac{1}{3},\frac{1}{2}\right) I_u^2 U_{\mathrm{avg}} \Rightarrow c_1 = \frac{U_{\mathrm{avg}}}{2}, \tag{50}$$

where $\beta(,)$ is the Beta function (see [1]). In the same way, c_2 and c_3 are

$$u^2_{\mathrm{rms},2} = (I_v U_{\mathrm{avg}})^2 = 2c_2 \int_0^\infty S_v(k)\,dk \approx 2c_2 \left[0.1189\,\beta\left(\frac{1}{2},\frac{4}{3}\right) + 0.3163\,\beta\left(\frac{1}{3},\frac{3}{2}\right)\right] I_v^2 U_{\mathrm{avg}} \Rightarrow c_2 = c_3 \approx \frac{U_{\mathrm{avg}}}{2}. \tag{51}$$

As can be observed in Fig. 2, the spectra of the simulated series fit well with the target spectra in the three principal directions; indicating that the anisotropy of the spectra is well represented by the proposed method. The rms value of each simulated fluctuating velocity component (obtained from a sample of 10 velocity simulations) is also compared to the corresponding target values. As shown in Table 1, the rms values of the fluctuating velocities simulated by the MDSRFG approach are in better agreement with the target values than those obtained using the *scaling and orthogonal transformation* or the *aligning and remapping* techniques [15].

When modeling the spatial correlation between same fluctuating velocity components in two different points i and j, a spatial correlation matrix needs to be computed. This target function is built for the u-component, for instance, from the spectra and coherence functions between nodes i and j as

$$\boldsymbol{S}_{\boldsymbol{c}\,i,j} = \sum_{m=1}^{M} \sqrt{Su^i(f_m) Su^j(f_m)}\,\gamma_u^y(f_m), \tag{52}$$

where

$$\gamma_u^y(f_m) = \exp\left(\frac{-C_u^y |y_i - y_j| f_m}{U_{\mathrm{avg}}}\right), \tag{53}$$

is the coherence function of the u fluctuating velocity component in the y-direction and C_u^y is the decay coefficient (usually taken in the range 10–12).

In Figs. 3–5 the spatial correlation for the u, v and w-components of the velocity fluctuations obtained by the expression (45) is compared to correlations computed using Eq. (52) for different values of L_s.

Time correlation is also computed for each velocity component according to the following expression (for the u-component for instance):

$$R(m\,\delta\tau) = \frac{1}{M-m} \sum_{j=0}^{M-m} u(j\,\delta\tau)\,u[(j+m)\,\delta\tau], \tag{54}$$

here m is an integer such that $\tau_m = m\,\delta\tau$, with $0 \leqslant m < M$, $\delta\tau$ is the time step size and M is the length of the vector τ_m. Samples of temporal correlations from the MDSRFG and the DSRFG methods are shown in Figs. 6–8 for each velocity component. Also, they are compared to the autocorrelation function of a random stationary process:

$$R_i(\tau) = e^{-|\tau|/T_i}, \tag{55}$$

with time scales T_i $(i = u, v, w)$ computed as

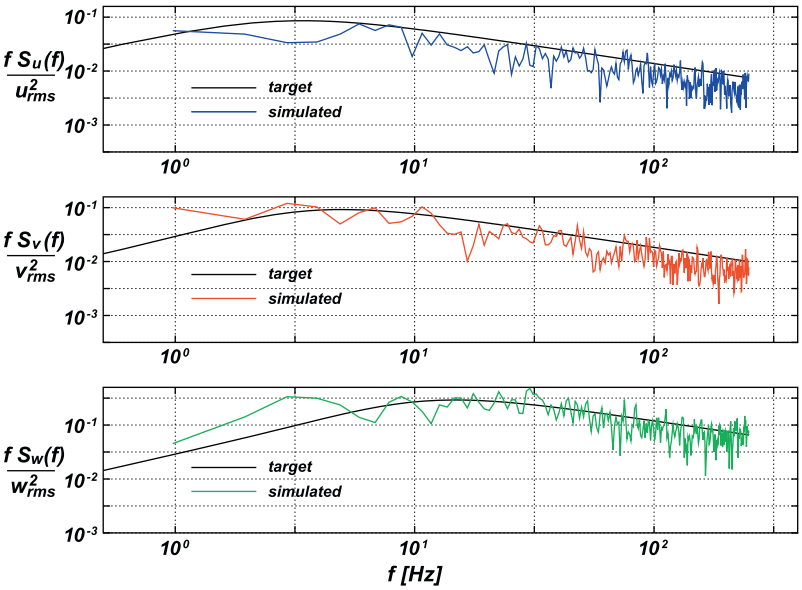

Fig. 2. Spectra of the velocity series simulated by the MDSRFG vs. target spectra.

Table 1
rms values (m/s) of the simulated velocities by different techniques.

	σ_u	σ_v	σ_w
Scaling and transformation	0.9968	2.44	2.9956
Aligning and remapping	0.95	1.9987	3.08
MDSRFG approach	1.0527	2.1850	3.1123
Target	1.12	2.24	3.36

$$T_i = \int_0^\infty R_i(\tau)\, d\tau \equiv \sum_{j=0}^{M_0} R_i(j\,\delta\tau)\,\delta\tau, \tag{56}$$

where $M_0 < M$. Low frequency fluctuations cause oscillations on the time correlation around the zero value as the time lag tends to infinite. Consequently, if Eq. (56) is approximated without an adequate upper limit of the sum, it will fail to estimate the scale [35]. In this work the time scale is computed by setting M_0 to the first τ-axis crossing value, see Figs. 6–8.

In order to analyze the influence of the time correlation parameter τ_0 on the time scales in the MDSRFG method, a parametric study is performed and the results are shown in Fig. 9 for each fluctuating velocity component. In the original test of Huang et al. [15] no time scale value was provided, whereby in this work it is estimated from Taylor's hypothesis: $T_i = L_i/U_{\text{avg}}$ $(i = u, v, w)$. These values are compared with those obtained by the MDSRFG and DSRFG methods, see Table 2.

The results in Fig. 9 and Table 2 correspond to the mean and standard deviation values of the time scale over a sample of 70 velocity series. The sample size is chosen as statistically representative of the velocity record. It is important to highlight here the possibility to slightly modify the time scale with different τ_0 values in the MDSRFG method whereas for the DSRFG method one are limitated to the three values shown in Table 2. Note that even the target time scales, estimated by the Taylor's hypothesis, are in accordance with those obtained by the DSRFG method, the application of the MDSRFG approach leads to a wider range of possible values by changing τ_0, see Fig. 9.

The anisotropic turbulence conditions at the inlet plane can be obtained by performing a previous RANS simulation or by experimental measurements. The two input parameters, L_s and τ_0, must be selected in order to reproduce the statistical properties of the flow under consideration. In this sense, the parameter θ_1 in Eq. (46) varies between 1 and 2 (see [15]) and τ_0 between 0.75 and 1.5, this later range of values being derived from the parametric analysis shown in Fig. 9. Within this range one can select the time scale values that better approximate the target ones without compromising other physical features (i.e., without loosing the adjustment of the velocity spectra, spatial correlation and rms values of the turbulent flow being simulated).

To validate the relationship proposed by Eq. (39) the influence of the frequency interval size Δf over the rms values of the time series is analyzed. What it is expected is that the synthetic turbulence generation provides the correct rms values as $\Delta f \to 0$, that is, as the discretization of the spectrum becomes finer the energy content in each frequency should be included in the time series generation. Table 3 shows the results of this analysis, where it can be seen that the method proposed in this work converges to the target values as Δf becomes smaller while in the case of the DSRFG method the values do not converge at all.

As it is clearly depicted by Eq. (38), the computational cost is identical as in the DSRFG method. Thus, for each node at the inlet section the cost at each time step is $O(MN)$; where M is the number of points in which the target spectrum is discretized

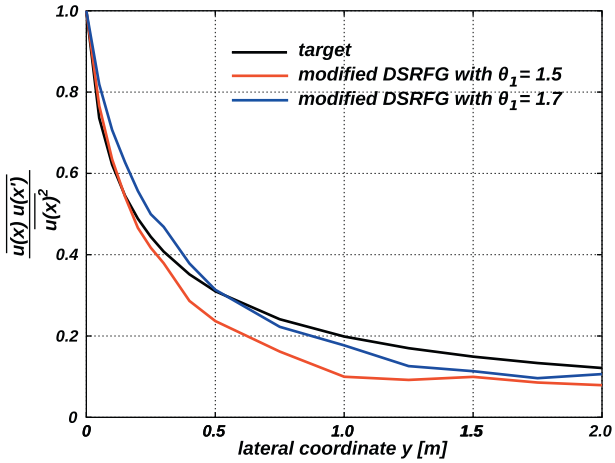

Fig. 3. Non-dimensional spatial correlation of the u fluctuating velocity component.

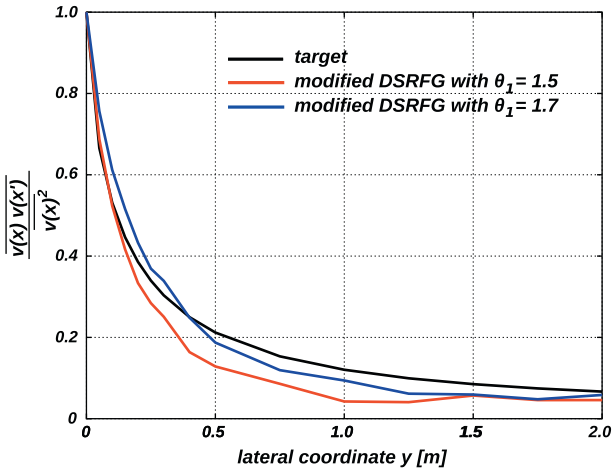

Fig. 4. Non-dimensional spatial correlation of the v fluctuating velocity component.

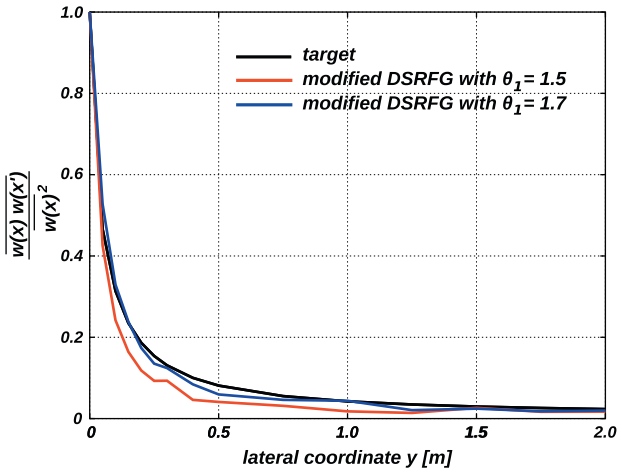

Fig. 5. Non-dimensional spatial correlation of the w fluctuating velocity component.

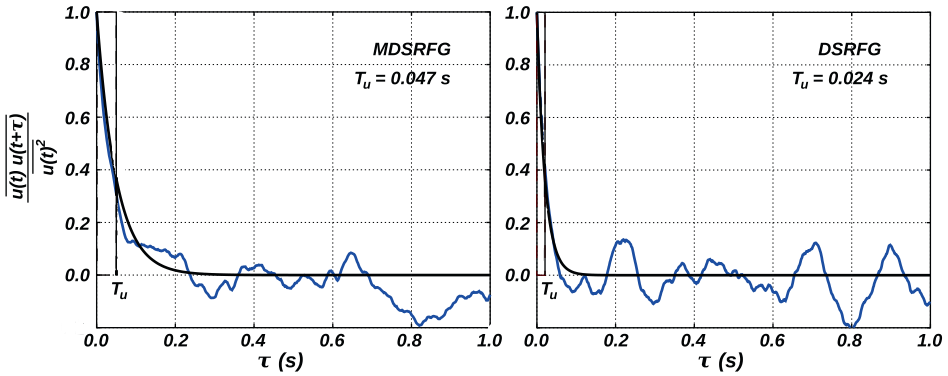

Fig. 6. u Velocity component non-dimensional time correlation. MDSRFG (*left*) and DSRFG method (*right*).

and N the number of samples for each wave number k_m. Furthermore, the computation of the fluctuating velocity components in Eq. (38) is independent of the LES process, i.e., the turbulence synthesis for some number of time steps (or the entire simulation process) can be done prior to the LES computations.

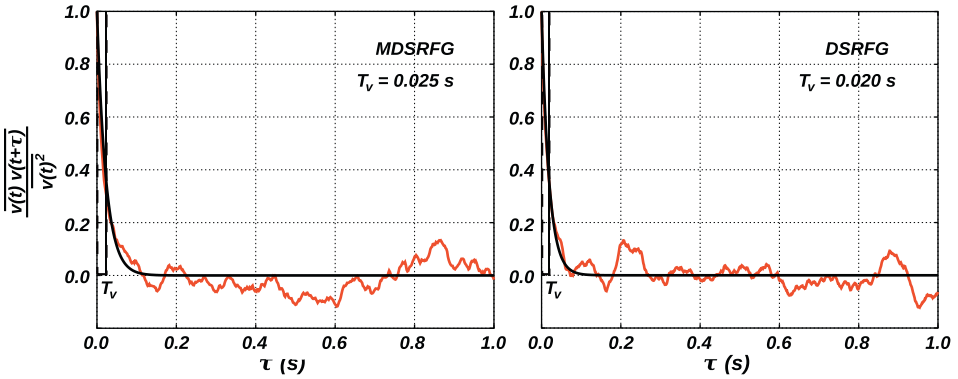

Fig. 7. v Velocity component non-dimensional time correlation. MDSRFG (*left*) and DSRFG method (*right*).

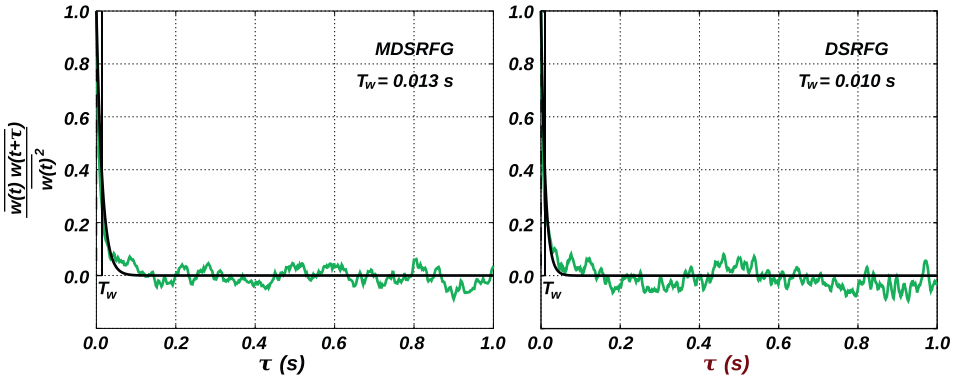

Fig. 8. w Velocity component non-dimensional time correlation. MDSRFG (*left*) and DSRFG method (*right*).

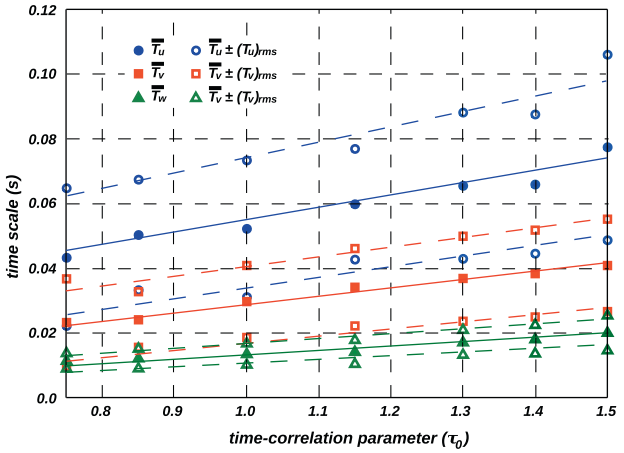

Fig. 9. Time scale statistics of the fluctuating velocity components as a function of τ_0 obtained by the MDSRFG method.

As a final observation, we notice that the proposed approach, as any synthesized turbulence generation method, must be used as a turbulence initializer, i.e., a perturbation generator that "triggers" the transition to a fully developed turbulence state by LES [9]. In this regard, it must be said that independently of the selected L_s value, the resolved scales are in concordance with the mesh (filter) size which is inherent to the LES conception.

Table 2
Time scale statistics comparison (s).

	T_u	T_v	T_w
DSRFG approach	0.034 ± 0.028	0.022 ± 0.009	0.010 ± 0.002
MDSRFG approach	0.043 ± 0.021	0.023 ± 0.014	0.011 ± 0.002
Target	0.043	0.021	0.007

Table 3
Comparison of the standard deviation values of the synthesized velocity components by the two methodologies.

Δf	σ_u		σ_v		σ_w	
	DSRFG	MDSRFG	DSRFG	MDSRFG	DSRFG	MDSRFG
10	0.49	0.76	1.27	1.84	2.05	2.95
5	0.83	0.87	1.93	2.07	2.94	3.01
2	1.47	0.98	3.15	2.11	4.69	3.03
1	2.17	1.04	4.47	2.11	6.75	3.11
Target	1.12		2.24		3.36	

5. Application of the modified DSRFG method in LES

It is well known that the generation of developed turbulence by LES at high Reynolds number flows is computationally expensive and time consuming. In order to avoid this drawbacks, the MDSRFG method can be used to setting up the turbulent inflow conditions in LES computations. In the following sections, two examples of application of the MDSRFG method are shown. For the sake of simplicity in the comparison between the DSRFG and MDSRFG approaches, both parameters θ_1 and τ_0 are set to 1.

The computational simulations were performed using PETSc-FEM (http://www.cimec.org.ar/petscfem) which is a general purpose, parallel, multiphysics finite element program that has been used in many applications including analysis of petroleum refinery processes, aerospace industry, environmental impact assessment and siderurgical processes [30,25]. PETSc-FEM uses the Finite Element Method (FEM) to solve the momentum and continuity equations for the velocity and pressure at each node and at each time step on unstructured meshes. Streamline-Upwind/Petrov–Galerkin (SUPG) [16,7] and the Pressure-Stabilizing/Petrov–Galerkin (PSPG) [33,34] discretization scheme of the incompressible Navier–Stokes equations were implemented.

5.1. Flow through a conical diffuser

This test case consists of a swirling boundary layer developing in a conical diffuser and was experimentally studied by Clausen et al. [8]. The conical diffuser is placed 100 mm downstream of a rotating swirl generator of diameter $D = 260$ mm and discharges into the atmosphere at $x = 510$ mm, see Fig. 10.

The device in charge of the swirl generation is a honeycomb positioned 500 mm before the beginning of the expansion which rotates with a part of the pipe of 400 mm long after it, while all other parts are locked. In the diffuser expansion, the boundary layer separation is prevented by the swirl which is strong enough to avoid recirculation in the core flow. The Reynolds number of the experimental test was 2.08×10^6 based on the diameter of the inlet section D, the mean axial velocity $U_x = 11.6$ m/s and the kinematic viscosity $\nu = 1.45 \times 10^{-6}$ m^2/s.

The computational domain adopted is shown in Fig. 11. A large dump is added in order to avoid recirculations in the diffuser outflow region. A structured mesh has been used for the computational simulation of the swirling flow which consists of 743,925 cells and 760,568 nodes.

Synthesized turbulence is imposed in all nodes at plane $x = -25$ mm considering the von Kármán spectra, Eqs. (47)–(49) and Fig. 12. At the dumper outlet boundary we impose $p = p_{\text{ref}}$, being $p_{\text{ref}} = 10,1325$ Pa the reference pressure. In Fig. 13 the comparison between the computational simulation for both, DSRFG and MDSRFG methods, and the ERCOFTAC measurement data (http://cfd.mace.manchester.ac.uk/ercoftac/) is shown. Clearly, the mean velocity (streamwise and orthoradial) and the kinetic energy boundary conditions for the MDSRFG method match the experimental data at the inlet. A frequency step $\Delta f = 10\ \text{s}^{-1}$ is enough for the MDSRFG method to provide a suitable turbulent kinetic energy while this is not the case for the DSRFG approach, as it can be seen in Fig. 13.

Vortex structures. Pictures of unsteady vortex structures were obtained from computational simulations by means of isosurfaces of the second invariant of the velocity gradient tensor. This is the so called Q-criterion, which can be written for an incompressible flow as [17]:

$$Q = \frac{1}{2}(\Omega_{ij}\Omega_{ij} - S_{ij}S_{ij}), \tag{57}$$

where S_{ij} is the rate-of-strain tensor and Ω_{ij} is the rate-of-rotation tensor which being the symmetric and antisymmetric parts of the velocity gradient tensor $A_{ij} = \partial u_i/\partial x_j$ respectively, i.e.,

$$S_{ij} = (A_{ij} + A_{ji})/2 \quad \text{and} \quad \Omega_{ij} = (A_{ij} - A_{ji})/2. \tag{58}$$

The physical interpretation of Eq. (57) is that the second invariant Q is a balance between the strain rate S_{ij} and the rotation rate Ω_{ij} which implies that positive Q isosurfaces exhibits zones where the amount of rotation exceeds the strain. Furthermore, Q can be expressed in a different form:

$$Q = \frac{1}{4}\left[\sigma^2 - 2(S_{ij}S_{ij})\right] = -\frac{1}{2}\frac{\partial u_i}{\partial x_j}\frac{\partial u_j}{\partial x_i} = -\frac{1}{2\rho}\nabla^2 p \tag{59}$$

where the connection between Q and the vorticity modulus (or enstrophy $\sigma^2 = \sigma_1^2 + \sigma_2^2 + \sigma_3^2$) arises. $\sigma_i, i = 1, 2, 3$ are the vorticity components in the three spatial directions and $\nabla^2 p$ is the Laplacian of the pressure. From this equation it is possible to prove that the Q-criterion ($Q > 0$) is a necessary condition for the existence of thin, convex low pressure-tubes (see the work of Dubief and Delcayre [12] for a detailed discussion about this subject). Vortex structures identified with $Q = 4000\ \text{s}^{-2}$ are shown in Fig. 14. It can be noted the instantaneous characteristic vortex structures of this model are well captured.

5.2. Ahmed body

The second test is a computational simulation of the flow around the Ahmed's body. The Ahmed body is a conceptual model of a generic car, proposed in the experimental work of Ahmed et al. [2]. Though this model is composed of three simple geometry parts: a fore body, a mid section and a rear end; the flow around it still retains some characteristics of the flow around real road vehicles. Fig. 15 shows the geometry of the model for a slant angle of 35°. All units are in millimeters.

Wind velocity and turbulence statistical parameters of the incident flow at the test section are shown in Table 4. Other parameters, like turbulence intensities $I_v = 0.02$, $I_w = 0.03$ and integral length scales $L_u = 0.3$, $L_v = 0.1$ and $L_w = 0.05$ were also adopted. The Reynolds number for the experimental test is roughly 1.70×10^6 based on the length of the vehicle model $L = 1.044$ m, the mean velocity magnitude 23.6 m/s, the kinematic viscosity $\nu = 1.45 \times 10^{-6}\ \text{m}^2/\text{s}$ and a constant density

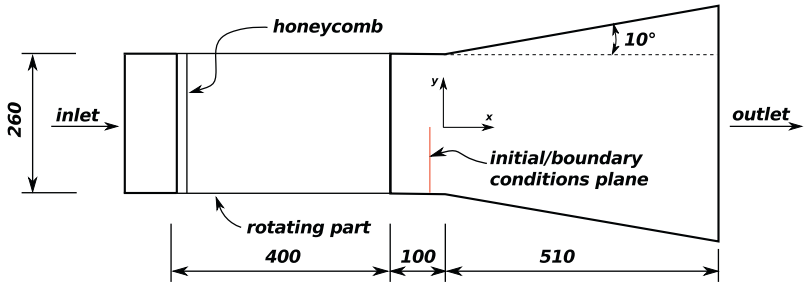

Fig. 10. Diffuser test case. All dimensions are in mm.

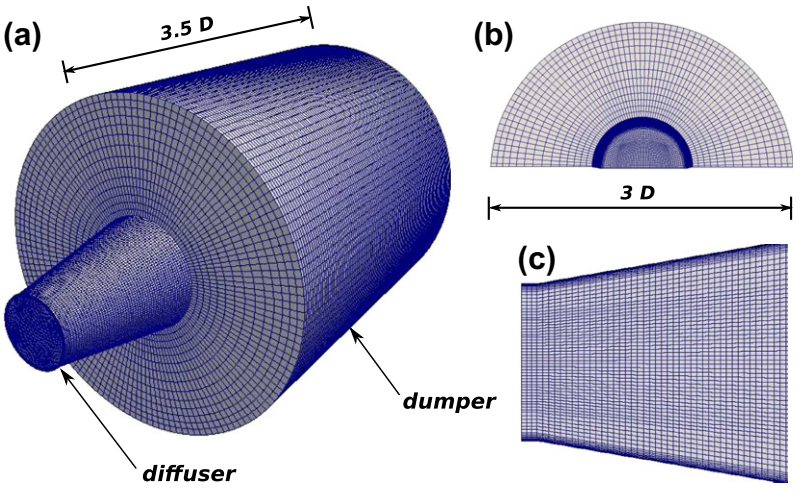

Fig. 11. Diffuser test case. All dimensions are in mm.

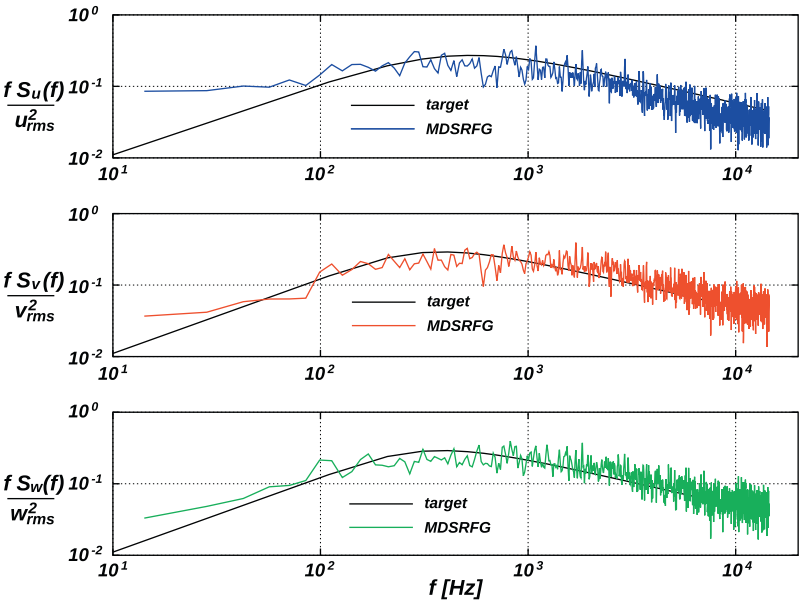

Fig. 12. Comparison of the spectra simulated by the MDSRFG with the target spectra.

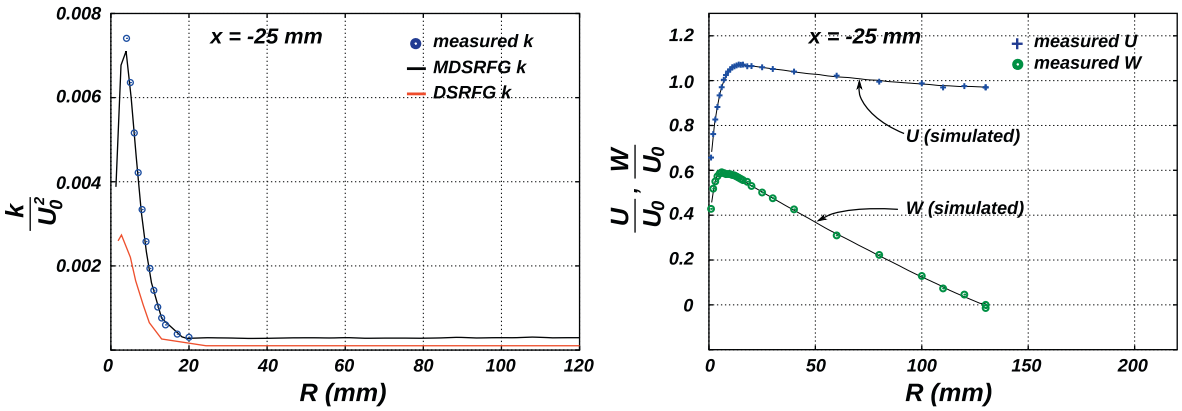

Fig. 13. Turbulent kinetic energy (*left*), mean streamwise and orthoradial velocity profile (*right*) obtained by the computational simulation and experimental data [8].

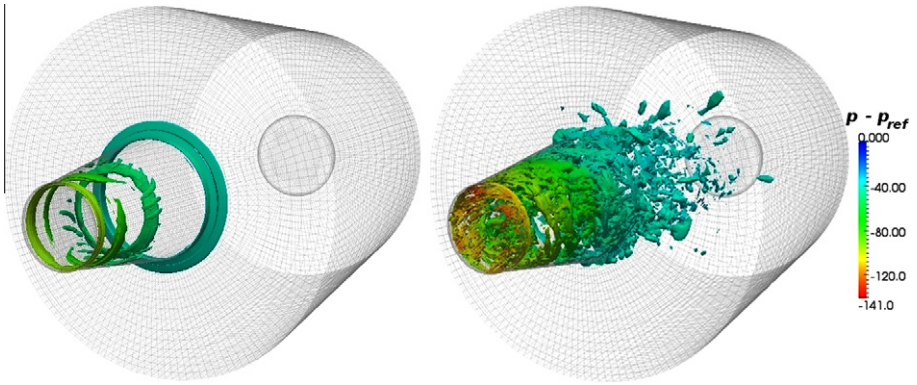

Fig. 14. Vortex flow structures ($Q = 4000\ s^{-2}$) colored by pressure (N/m^2). Computational simulation with no synthesis (*left*) and with the MDSRFG method (*right*).

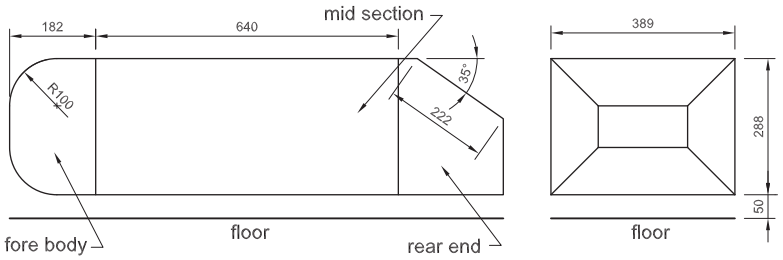

Fig. 15. Ahmed model.

Table 4
Parameters for the inflow boundary condition at the wind tunnel test section [37].

z [cm]	u_1^+	I_u	σ_u
2.5	0.74	0.096	1.677
7.0	0.83	0.070	1.372
17.0	0.92	0.045	0.978
22.5	0.95	0.027	0.606
30.0	0.98	0.011	0.255
40.0	0.982	0.008	0.186
48.0	0.985	0.007	0.163
57.5	0.986	0.0065	0.151
62.5	0.987	0.007	0.163
70.0	0.988	0.008	0.187
75.0	0.988	0.009	0.210
88.0	0.990	0.010	0.234
102.5	0.995	0.011	0.258
119.0	1.000	0.012	0.283

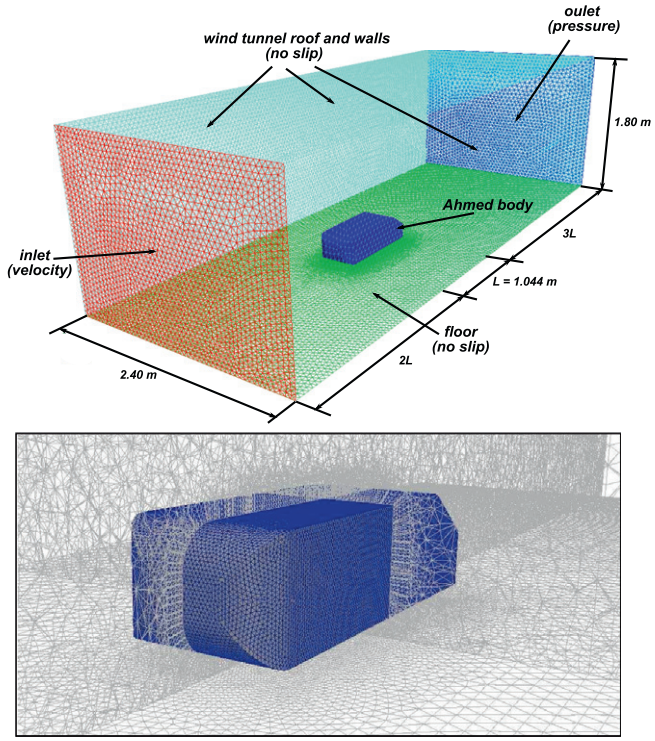

Fig. 16. Computational domain and detail of the mesh.

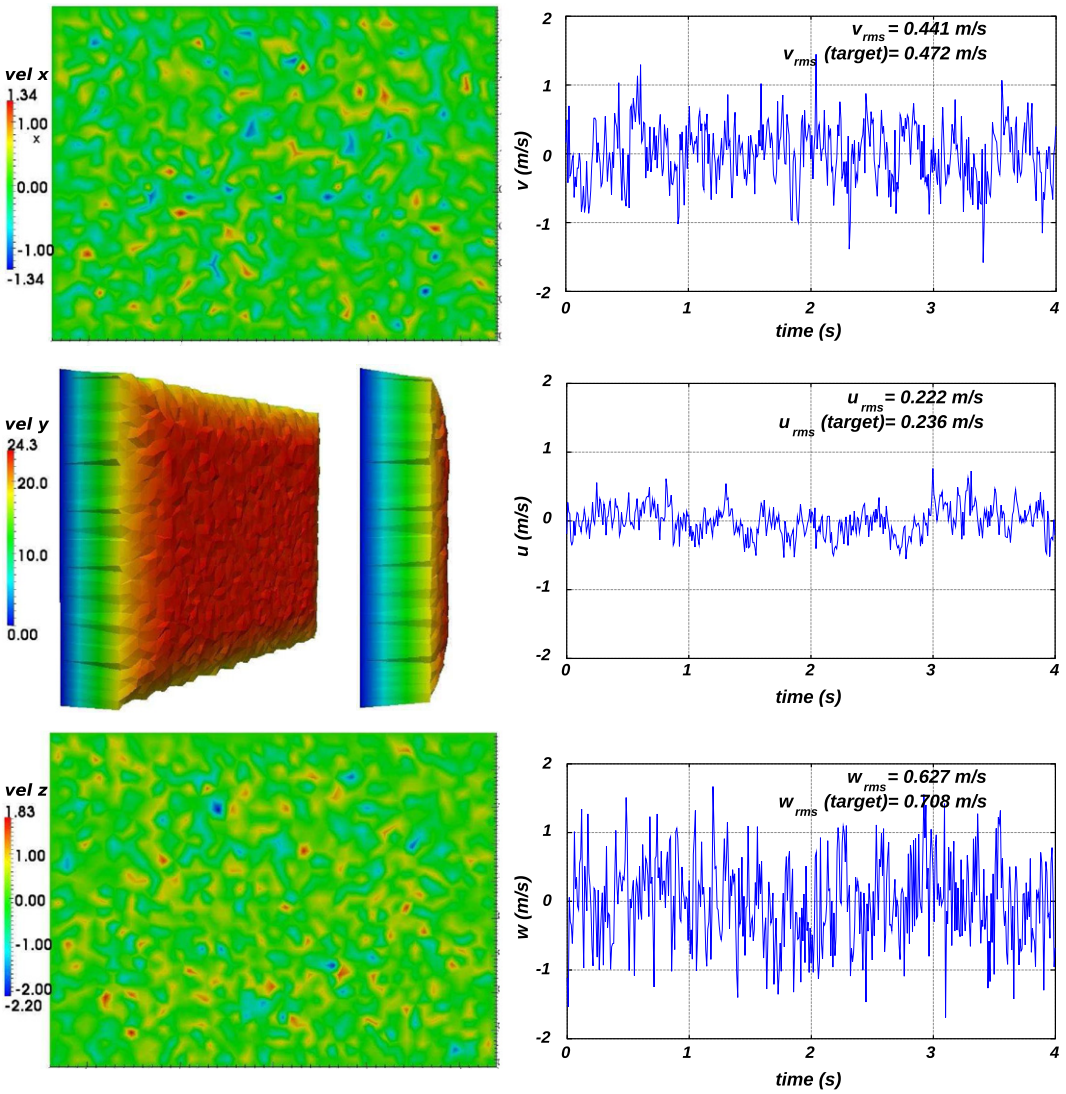

Fig. 17. Inlet fluctuating velocities simulated by the MDSRFG method.

Table 5
rms values (m/s) of the velocity series simulated with $\Delta f = 0.5\ s^{-1}$.

	σ_u	σ_v	σ_w
DSRFG	0.4432	0.9043	1.2228
MDSRFG	0.2219	0.4411	0.6272
Target	0.236	0.472	0.708

$\rho = 1.225\ kg/m^3$. In order to address the accuracy of the DSRFG and MDSRFG methods, a small frequency interval, $\Delta f = 0.5\ s^{-1}$, was used in both approaches.

The computational domain is a rectangular box with a cross section of 2.40 m width (x-direction) and a height of 1.80 m (z-direction) representing a wind tunnel section, see Fig. 16. The body was located at $2L$ downstream (y-direction) the inlet section and at $3L$ upstream the outlet boundary to allow full development of the flow downstream to the model, totaling an extension of $6L$. Non-slip boundary condition is prescribed at ground, roof and tunnel walls, while null pressure is imposed at the outlet wall. With these conditions the blockage ratio is about of 2.6%.

The grid was refined close to the body surface in order to account for viscous effects at the walls and to adequately capture the changes in flow variables within the boundary layer region. Five rows of wedge type elements, shown in detail in

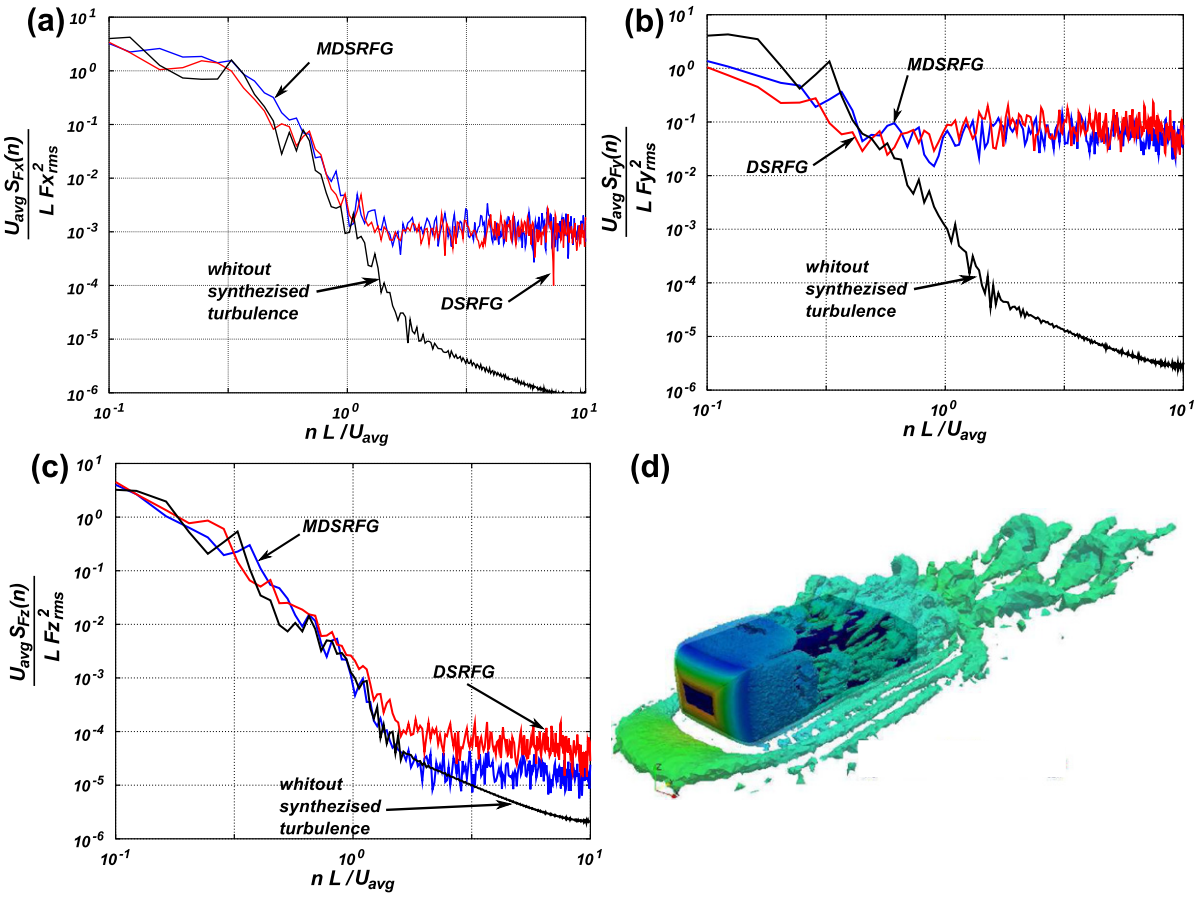

Fig. 18. Computational simulation with inlet synthesized turbulence (MDSRFG and DSRFG) and without inlet synthesized turbulence. (a) Side force spectrum (x-component force). (b) Drag force spectrum (y-component force). (c) Lift force spectrum (z-component force). (d) $Q = 800\ s^{-2}$ isosurface colored by pressure.

Fig. 16, were generated from the surface of the vehicle model. The first wedge-layer has a thickness $h_m = 4.79 \times 10^{-3} L = 5$ mm. A classical logarithmic law for velocity was imposed at the body surface (see Ref. [27]).

Fig. 17 shows, in the right side, the time history of the simulated fluctuating velocity components by the MDSRFG method in a central point of the inlet section and the instantaneous fluctuation contours on the left side. The velocities maintain the spatial anisotropy among the three directions, as can be observed from the statistical values. Furthermore, the rms values of the simulated velocity series are compared in Table 5. Clearly, for the small value of Δf considered, the MDSRFG values almost perfectly agrees with those of the target while in the case of the DSRFG method the rms values exceeds the target ones.

5.2.1. Forces acting on the body

To characterize the transient behavior of the forces acting on the model, an analysis in the frequency domain is performed. In Fig. 18 the spectra of the forces in the z, x and y directions are shown. It can be seen that for the x and y-directions the energy content of the fluctuating forces obtained with the application of the DSRFG and MDSRFG methods are in agreement. The lift-force spectrum shows different results for reduced frequency values higher than unity.

Also in Fig. 18 instantaneous vortex structures identified with $Q = 800\ s^{-2}$ are shown. It can be noted that these structures are in correlation with those reported by Uruba [36].

5.2.2. Unsteady velocity

The velocity unsteadiness produced by the application of the DSRFG method is relatively higher than the one obtained with the MDSRFG method as a consequence of the higher kinetic energy provided by the former approach. This is observed in the wake along the plane of symmetry, Fig. 19, and in the rms values of pressure coefficient on the model back-light, see Fig. 20.

The pressure coefficient unsteadiness is computed as

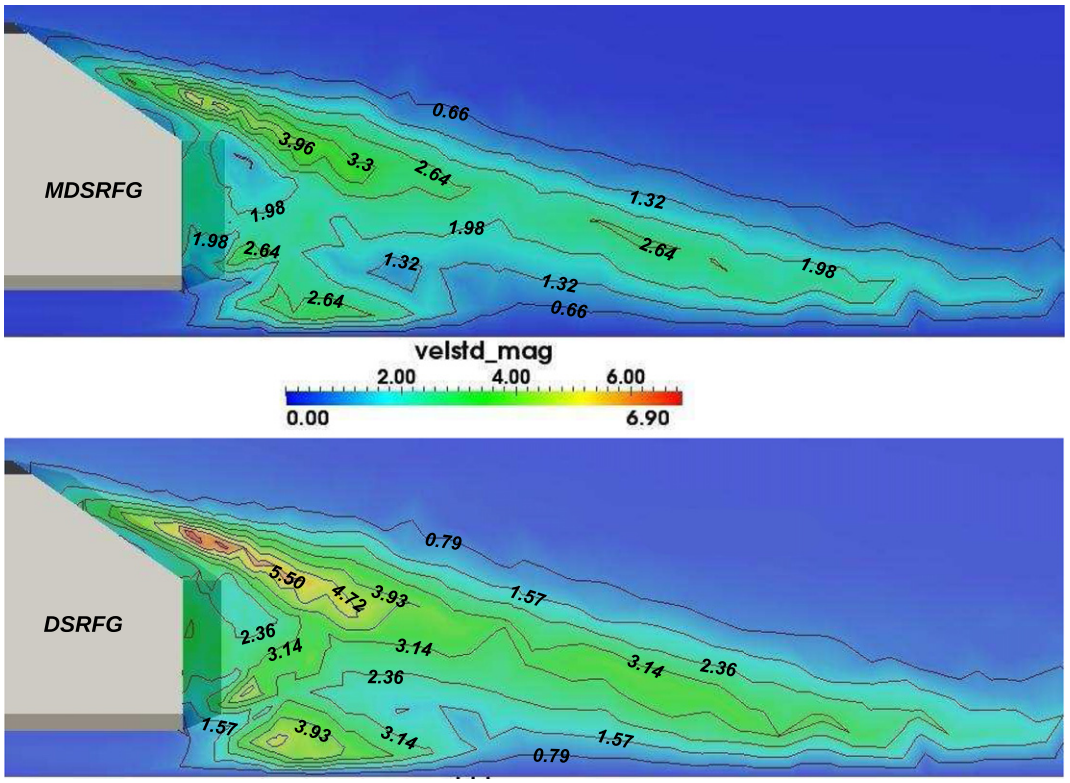

Fig. 19. Standard deviation velocity magnitude. ***Top***: MDSRFG and ***bottom***: MDSRFG.

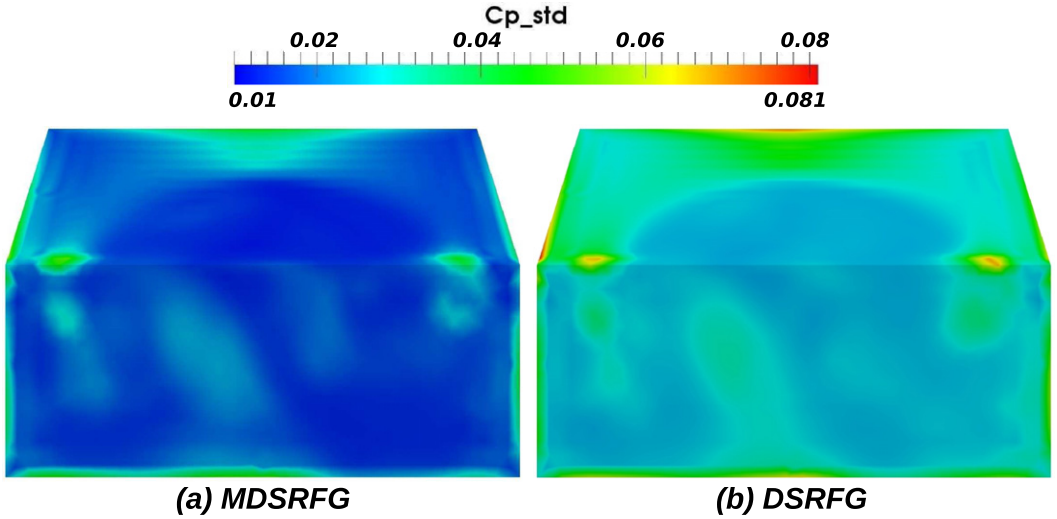

Fig. 20. Standard deviation of the pressure coefficient on the model back-light.

$$\sigma_{C_p} = \frac{\sigma_p}{\frac{1}{2}\rho U_{\text{avg}}^2} \tag{60}$$

and although different levels of unsteadiness induced by both synthesized turbulence methods are evident, the distribution of the pressure coefficient unsteadiness on the back-light of the model presents in both cases high similarities, such as the wide region of low fluctuating values in most parts of the vertical base and in the central region of the slant.

Regions of high unsteadiness values on the sides of the back-light surface (near the edge of intersection of the slant and vertical base) were detected in both cases. These spots are consistent with the observed vortex generating regions in

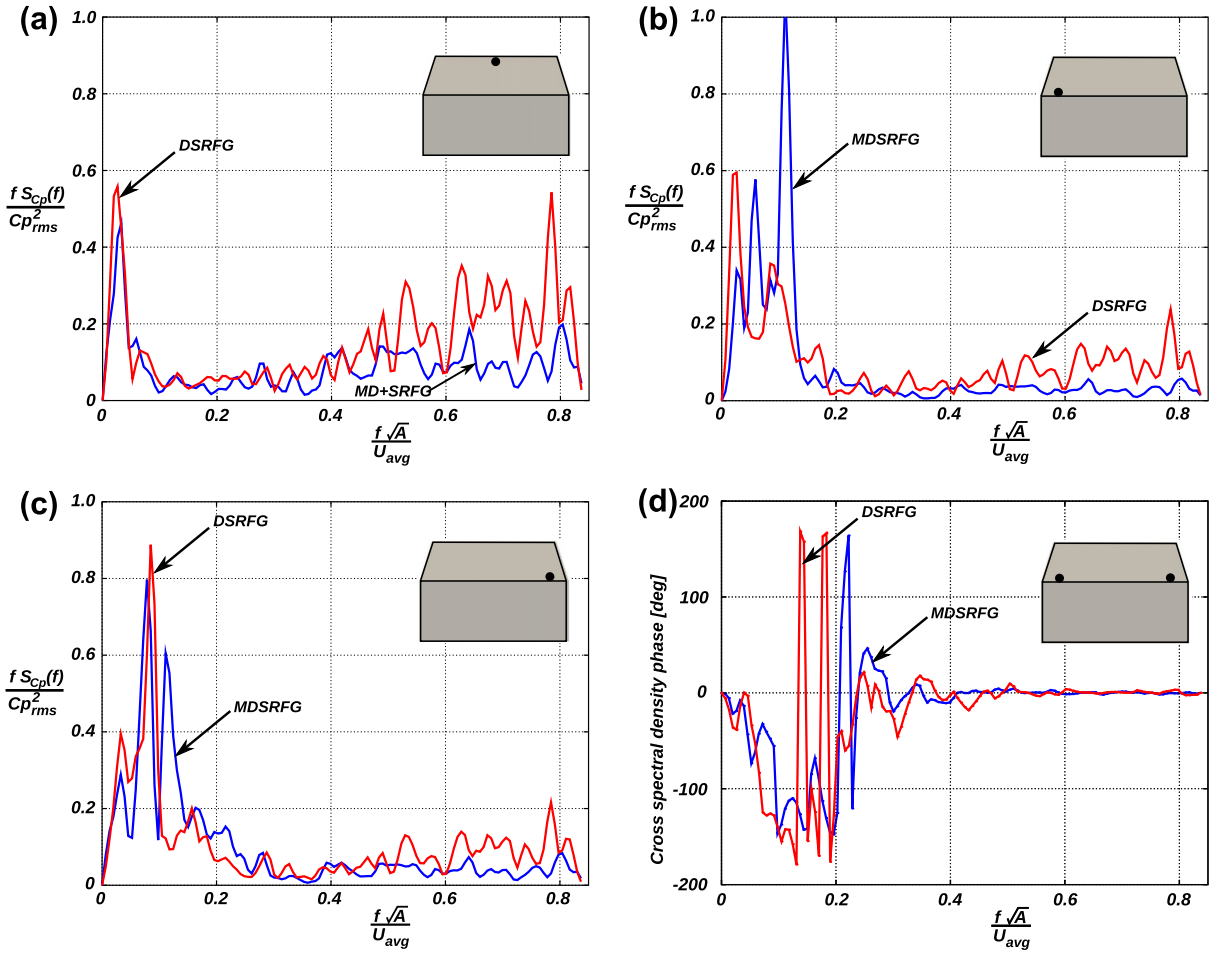

Fig. 21. Cross spectral density phase between two points on the back-light of the model.

Fig. 18(d). Another region of high unsteadiness activity was found near the top edge of the back-light slant surface in coincidence with the flow separation zone.

Furthermore, a frequency domain study of the pressure behavior was performed. Fig. 21 shows the non-dimensional auto-spectral density measured in points located on the regions previously highlighted, by the simulations with the DSRFG and MDSRFG methods. In can be seen that in the spots analyzed, higher energies are detected in the range of high Strouhal numbers in the simulation with DSRFG. For the low Strouhal numbers the energies are quite similar (except for the case in Fig. 21(b) where the energy content in the simulation with MDSRFG is higher) denoting that both methods maintain the mean characteristics unaffected. Also, this low-Strouhal number region ($f\sqrt{A}/U_{\text{avg}} < 0.2$, based on the square root of model frontal area) possesses the higher energy content which can be associated with the presence of shedding phenomena.

In Fig. 21 the phase correlation between the points in the regions of vortices production is shown. It can be seen that the phase estimate for Strouhal numbers lower than 0.2 presents a phase shift of about 100° and more, indicating a nearly alternate shedding.

6. Conclusions

In this paper, a general method for the generation of inflow synthesized turbulence has been introduced and evaluated. The method is based on a previous turbulence generator known as the discretizing and synthesizing random flow generation (DSRFG) method. The proposed approach preserves the main characteristics and advantages of the DSRFG method: it is highly parallelizable, different spectral models can be used and it can represent either isotropic and anisotropic turbulence. In addition, the key point of the modified DSRFG (MDSRFG) method is that it preserves the statistical quantities that could be prescribed at the inlet of the domain as the number of samples M (number of points in the spectrum) increases, through the computation of the factors $p_i^{m,n}$ and $q_i^{m,n}$ by Eqs. (42) and (43). This characteristic ensures that the imposed turbulence intensity on the fluctuating velocity series represents adequately the kinetic energy of the turbulent flow under study.

Following previous methodologies [28,5], a dimensionless time scale parameter, τ_0, has been included in the formulation of the proposed approach in order to "control" the time correlation of the generated velocity series. In this way, the MDSRFG method can modify the time scale by varying τ_0 as it has been demonstrated in Section 4.

Some numerical tests show that the proposed approach is very well-suited for three-dimensional computations using the LES approach. For the swirling turbulent flow inside a diffuser the inlet conditions obtained matches almost exactly the experimental measurements. Regarding to the simulation of the flow over the Ahmed body, it has been shown that results obtained, i.e., forces, level of unsteadiness in the wake and the back-light of the model, are very sensitive to the upstream inflow conditions and therefore this issue must be correctly addressed by any synthesized turbulence method.

Acknowledgments

This work has received financial support from *Consejo Nacional de Investigaciones Científicas y Técnicas* (CONICET, Argentina, Grant PIP 5271/05), *Universidad Nacional del Litoral* (UNL, Argentina, Grant CAI+D 2009 65/334), *Agencia Nacional de Promoción Científica y Tecnológica* (ANPCyT, Argentina, Grants PICT 2492/2010, PICT 01141/2007, PICT 0270/2008, PICT-1506/2006), *Universidad Tecnológica Nacional, Facultad Regional Resistencia* (UTN FRRe, Argentina, Grant PID 2012 25/L057).

References

[1] M. Abramowitz, I. Stegun, Handbook of Mathematical Functions: With Formulas, Graphs, and Mathematical Tables, Dover Publications, 1970.
[2] S.R. Ahmed, G. Ramm, G. Faltin, Some salient features of the times-averaged ground vehicle wake, vol. 1, Society of Automotive Engineering, Inc., 1984, p. 131.
[3] M.H. Baba-Ahmadi, G. Tabor, Inlet conditions for LES using mapping and feedback control, Computers & Fluids 38 (2009) 1299–1311.
[4] G.K. Batchelor, The Theory of Homogeneous Turbulence, Cambridge University Press, 1982.
[5] P. Batten, U. Goldberg, S. Chakravarthy, Interfacing statistical turbulence closures with large-eddy simulation, AIAA Journal 42 (2004) 485.
[6] J.S. Bendat, A.G. Piersol, Measurement and Analysis of Random Data, John Wiley & Sons, Inc., 1967.
[7] A. Brooks, T. Hughes, Streamline upwind/Petrov–Galerkin formulations for convection dominated flows with particular emphasis on the incompressible Navier–Stokes equations, Computer Methods in Applied Mechanics and Engineering 32 (1982) 199–259.
[8] P.D. Clausen, S.G. Koh, H. Wood, Measurements of a swirling turbulent boundary layer developing in a conical diffuser, Experimental Thermal and Fluid Science 6 (1993) 3948.
[9] L. Davidson, Using isotropic synthetic fluctuations as inlet boundary conditions for unsteady simulations, Advances and Applications in Fluid Mechanics 1 (1) (2007) 1–35.
[10] L. di Mare, M. Klein, W.P. Jones, J. Janicka, Synthetic turbulence inflow conditions for large-eddy simulation, Physics of Fluids 18 (2) (2006) 025107.
[11] P. Druault, S. Lardeau, J-P. Bonnet, F. Coiffet, J. Deville, E. Lamballais, J.F. Largeau, L. Perret, Generation of three-dimensional turbulent inlet conditions for large-eddy simulation, AAIA Journal 42 (3) (2004) 447–456.
[12] Y. Dubief, F. Delcayre, On coherent-vortex identification in turbulence, Journal of Turbulence 1 (11) (2000).
[13] P.A. Durbin, B.A. Pettersson-Reif, Statistical Theory and Modeling of Turbulent Flow, John Wiley & Sons Ltd., 2001.
[14] Fluent Inc., Fluent 12 User's Guide, 2010.
[15] S.H. Huang, Q.S. Li, J.R. Wu, A general inflow turbulence generator for large eddy simulation, Journal of Wind Engineering and Industrial Aerodynamics 98 (2010) 600–617.
[16] T. Hughes, A. Brooks, A multi-dimensional upwind scheme with no crosswind diffusion, in: Finite Element Methods for Convection Dominated Flows, vol. 34, ASME, 1979, pp. 19–35.
[17] J.C.R. Hunt, A.A. Wray, P. Moin, Eddies, stream and convergence zones in turbulent flows, Center for Turbulence Research Report, CTR-S88, 1988, pp. 193–208.
[18] J. Kim, P. Moin, R. Moser, Turbulence statistics in fully developed channel flow at low Reynolds number, Journal of Fluid Mechanics 177 (1987) 133–166.
[19] M. Klein, A. Sadiki, J. Janicka, A digital filter based generation of inflow data for spatially developing direct numerical or large eddy simulations, Journal of Computational Physics 186 (2003) 652–665.
[20] K. Kondo, S. Murakami, A. Mochida, Generation of velocity fluctuations for inflow boundary condition of LES, Journal of Wind Engineering and Industrial Aerodynamics 67 & 68 (1997) 51–64.
[21] R.H. Kraichnan, Diffusion by a random velocity field, The Physics of Fluids 13 (1970) 22–31.
[22] S. Lee, S. Lele, P. Moin, Simulation of spatially evolving turbulence and the applicability of Taylor's hypothesis in compressible flow, Physics of Fluids A 4 (1992) 1521–1530.
[23] K. Liu, R.H. Pletcher, Inflow conditions for the large eddy simulation of turbulent boundary layers: a dynamic recycling procedure, Journal of Computational Physics 219 (2006) 1–6.
[24] T.S. Lund, X. Wu, K.D. Squires, Generation of turbulent inflow data for spatially-developing boundary layer simulations, Journal of Computational Physics 140 (1998) 233–258.
[25] R.R. Paz, N.M. Nigro, M.A. Storti, On the efficiency and quality of numerical solutions in CFD problems using the Interface Strip Preconditioner for domain decomposition methods, International Journal for Numerical Methods in Fluids 52 (1) (2006) 89–118.
[26] L. Perret, J. Delville, R. Manceau, J.-P. Bonnet, Generation of turbulent inflow conditions for large eddy simulation from stereoscopic PIV measurements, International Journal of Heat and Fluid Flow 27 (2006) 576–584.
[27] W. Rodi, Comparison of LES and RANS calculation of the flow around bluff bodies, Journal of Wind Engineering and Industrial Aerodynamics 69–71 (1997) 55–75.
[28] A. Smirnov, S. Shi, I. Celik, Random flow generation technique for large eddy simulations and particle-dynamics modeling, Journal of Fluids Engineering 123 (2001) 359–371.
[29] A. Smirnov, I. Celik, S. Shi, LES of bubble dynamics in wake flows, Computers & Fluids 34 (2005) 351–373.
[30] M.A. Storti, N.M. Nigro, R.R. Paz, L.D. Dalcín. PETSc-FEM: a general purpose, parallel, multi-physics FEM program, 1999–2012. http://www.cimec.org.ar/petscfem.
[31] G.R. Tabor, M.H. Baba-Ahmedi, Inlet conditions for large eddy simulation: a review, Computers & Fluids 39 (2010) 553–567.
[32] H. Tennekes, J.L. Lumley, A First Course in Turbulence, MIT Press, 1970.
[33] T. Tezduyar, Stabilized finite element formulations for incompressible flow computations, Advances in Applied Mechanics 28 (1992) 1–44.
[34] T. Tezduyar, S. Mittal, S. Ray, R. Shih, Incompressible flow computations with stabilized bilinear and linear equal order interpolation velocity–pressure elements, Computer Methods in Applied Mechanics and Engineering 95 (1992) 221–242.
[35] A. Thacker, S. Loyer, S. Aubrun, Comparison of turbulence length scales assessed with three measurement systems in increasingly complex turbulent flows, Experimental Thermal and Fluid Science 34 (2010) 638645.

[36] V. Uruba, Lateral vortex dynamics behind Ahmed body, Proceedings of Applied Mathematics and Mechanics 10 (2010) 455–456.
[37] A. Wittwer, S. Möller, Characteristics of the low speed wind tunnel of the UNNE, Journal of Wind Engineering and Industrial Aerodynamics 84 (2000) 307–320.
[38] Z.-T. Xie, I.P. Castro, Efficient generation of inflow conditions for large eddy simulation of street-scale flows, Flow, Turbulence and Combustion 81 (3) (2008) 449–470.